Modeling of Ingot Distortions During Direct Chill Casting of Aluminum Alloys

J.-M. DREZET and M. RAPPAZ

A comprehensive three-dimensional (3-D) mathematical model based upon the ABAQUS software has been developed for the computation of the thermomechanical state of the solidifying strand during direct chill (DC) casting of rolling sheet ingots and during subsequent cooling. Based upon a finite-element formulation, the model determines the temperature distribution, the stresses, and the associated deformations in the metal. For that purpose, the thermomechanical properties of the alloy have been measured up to the coherency temperature using creep and indentation tests. The thermophysical properties as well as the boundary conditions associated with the lateral water spray have been determined using inverse modeling. The predicted ingot distortions, mainly, "butt curl," "butt swell," and lateral faces pull-in, are compared with experimental measurements performed during solidification and after complete cooling of the ingot. Particular emphasis is placed on the nonuniform contraction of the lateral faces. The influence of the mold shape and the contributions to this contraction are assessed as a function of the casting conditions.

I. INTRODUCTION

A schematic representation of the direct chill (DC) semicontinuous casting process is shown in Figure 1. For reasons of symmetry, only one quarter of the casting is shown. At the start of the process, liquid metal is poured in an open rectangular mold over a movable bottom block. As this block is moved downward, the metal is cooled first by contact with the mold (primary cooling) and second by the water-cooling sprays (secondary cooling). Direct chill casting proceeds in three main stages:[1] the start phase, during which the temperature field, the solidification front, the ingot shape, and the liquid metal–air interface (meniscus) change with time (nonstationary phase); the pseudostationary phase; and the end phase, during which liquid pouring is stopped and the ingot cools down. During processing, the ingot is subject to many distortions that arise as a consequence of combined thermal and mechanical effects.

A. *Butt Curl and Swell*

During the start phase, the ingot experiences a higher cooling rate than during the steady-state regime. Indeed, at the start of the drop, the ingot butt is chilled both by the bottom block and by the mold. As the block is moved down, the ingot is also cooled by the lateral water spray. This rapid chilling generates excessive thermal stresses that result in the bow of the first section of the ingot. This phenomenon is called "butt curl."[2,3] Butt curl is a major problem[4] because it reduces the rigid standing of the ingot on the starter block and causes a portion of the ingot to lose contact with the bottom block, leading to possible shell remelting. Moreover, water can enter the gap between the starting block and the underside of the ingot; its rapid vaporization may lead to a "bumping" of the ingot. Eventually, the thermally induced stresses and strains can form cracks and hot tears. Carrupt and Moulin[5,6] demonstrated that the decisive criterion in controlling butt curl is not its final value but its rate of evolution. Several solutions, such as injecting liquid CO_2 into the cooling water system[3] or using pulsed water to diminish the cooling during start-up,[4] were suggested to reduce butt curl. However, the start phase of DC casting of aluminum alloys still remains the most critical period of the process.

"Butt swell" is associated with a thicker section of the butt of the ingot as compared with the rest of the slab. During the start phase, the depth of the liquid pool is much smaller than during the stationary phase, as a result of both the reduced casting speed and the partial cooling by the bottom block. Thus, the ingot contraction is also reduced and the slab has nearly the same nominal dimensions as the mold. This situation is in fact similar to casting a metal in a permanent mold. However, once the starting phase is over, the sump deepens and the associated contraction of the slab increases, about 45 mm for a 510-mm-wide slab, *i.e.*, about 9 pct in pull-in (*i.e.*, in relative displacement[7]), at the midcenter of the lateral faces. Therefore, it appears as if the foot of the final slab had swollen, but it is in fact a reduced contraction caused by the thermal conditions during the start phase. This butt swell requires additional scalping before further processing of the ingot.

B. *Steady-State Inward Pull-In of the Rolling Faces*

After about 1 m of casting, a nearly steady-state regime is established for the thermal field. Under pseudo–steady-state conditions, the solidified shell contracts inward (*i.e.*, toward the liquid pool), but not uniformly throughout the ingot cross section. If a rectangular mold/inductor is employed, the lateral faces of the resulting ingot are concave ("bone shape"). To compensate for the larger pull-in measured at the center of the rolling faces, the sides of the mold are designed with a convex shape, usually with three linear segments.[7] At the present time, the mold geometry is designed by a trial-and-error method. Each significant change,

J.-M. DREZET, Graduate Student, and M. RAPPAZ, Professor, are with the Laboratoire de Metallurgie Physique, Ecole Polytechnique Federale de Lausanne, CH-1015 Lausanne, Switzerland.

Manuscript submitted December 8, 1995.

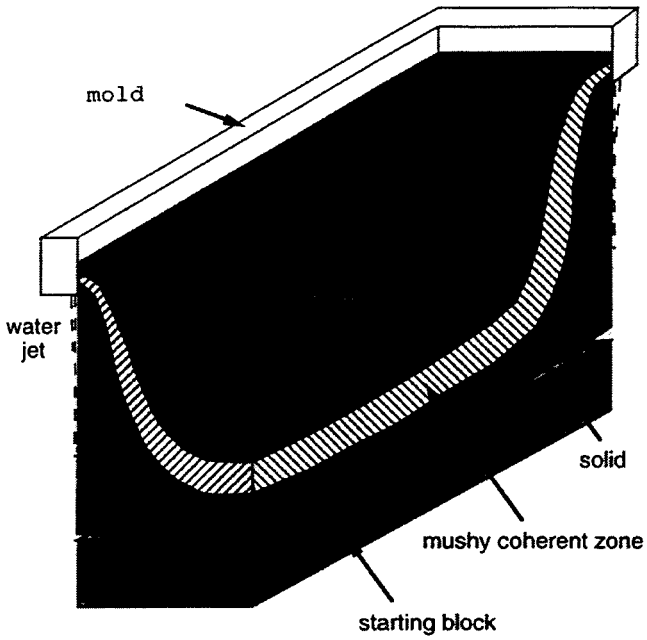

Fig. 1—Schematic view of the DC casting process. For symmetry reasons, only one-fourth of the casting is shown.

such as the alloy being cast, or the size of the ingot, requires considerable experimentation before an appropriate new casting procedure, starting block, and mold can be adopted. Consequently, development time and costs are still very high, especially when ingots of large section are to be cast.

The deformation of the ingot cross section during the stationary regime of semicontinuous DC casting and the mold design required to produce flat sheet ingots have been studied by Weaver.[8,9] Without giving a physically based explanation of this deformation, Weaver proposed an empirical model based on casting trials to predict the cross-sectional changes of DC cast ingots under the assumption of radial heat extraction. Weaver also showed that the mold design required to produce flat ingots changed from a two-straight-lines shape to an almost sinusoidal shape, and eventually to a three-straight-lines shape when the aspect ratio of the ingot (width over thickness ratio) was increased.[9] Drezet *et al.*[7] investigated the deformation of the cross section of the ingot during DC and electromagnetic castings and concluded that the pull-in of the rolling faces was about the same for the non–heat-treatable alloys of the 1*xxx*, 3*xxx*, and 5*xxx* series. They also showed that the 9 pct contraction of the lateral faces center was mainly a result of the inward bending of the solid shells induced by the thermal stresses.

C. *Ending Phase*

At the end of casting, liquid metal is no longer poured and the descent of the bottom block is stopped. As a result of this transient temperature evolution, the lateral faces pull-in is also reduced in a way similar to the butt swell.

D. *Thermomechanical Models*

With the development of powerful numerical methods and computers, mathematical models for the simulation of fluid flow, heat flow, and stress generation in a solidifying piece are being used increasingly in order to better understand, optimize, and design casting processes.[10–13]

Several modeling investigations have been carried out for the study of continuously cast steel ingots. Special attention has been paid to the thermal-stresses generation in the early stage of solidification and to the associated air-gap formation[14,15] as well as to the bulging of the strand induced by the ferrostatic head pressure.[16] Thomas *et al.*[17] developed a two-dimensional finite-element model to predict first the thermal history and then the associated stress generation in a static-cast steel ingot. The continuous casting of steel was studied by Williams *et al.*[18] These authors used an elasto-viscoplastic constitutive relationship for the calculations of the stresses in a metal cross section as it passes through the mold and then into the region where the surface is cooled by water sprays. Kelly *et al.*[19] presented a mathematical model for the computation of the thermomechanical state of a continuously cast steel ingot and studied the influence of the mold taper.

Modeling of the continuous casting process in the nonferrous metal industry[20] has usually been separated into two distinct, but interrelated tasks: that of modeling the thermal conditions in the ingot during casting and that of calculating the stress state in the ingot during and after casting. The coupling between thermal and mechanical effects is particularly strong during the start phase: high thermal gradients induce thermal stresses that deform the ingot, and in turn these deformations modify the heat extracted through the starting block or the mold. The start phase of DC casting of aluminum slabs has been studied by Hannart *et al.*[21] These authors computed the thermal stresses in three dimensions, with special emphasis on the induced strains, which play a major role in the initiation of cracks and butt-curl formation. Fjaer and Jensen[22] recently studied the influence of the starter block shape on the butt deformation of sheet ingots, whereas Jensen and Schneider[23] investigated experimentally and numerically the effect of various casting parameters on the crack tendency. During the start-up phase of electromagnetic (EM) casting, butt curl is particularly critical because the meniscus can be destabilized in the electromagnetic field, leading to a premature cessation of the casting process.[24] Mariaux *et al.*[25] developed a two-dimensional numerical model that fully coupled thermal aspects with mechanical effects and computed butt curl during the EM casting start phase.

Drezet *et al.*[7] investigated the mechanical interactions among the initially formed thin solid shell, the mold, and the metallostatic head during the steady-state regime of DC casting. By measuring the lateral faces pull-in during casting, they showed that the large contraction of about 9 pct of the ingot cross section was a result of the thermally induced stresses. They also made clear that a pull-in of 9 pct should not be interpreted as a contraction of 9 pct, because the solid shell undergoes bending during cooling. Different degrees of sophistication in treating the plastic deformation of the metal and different numerical methods were used to compute the stress generation during semicontinuous casting. Moriceau[26] and Janin[27] used a temperature-dependent elastoplastic model to simulate the stress generation and to study the hot-cracking tendency inside DC cast round billets. Mathew and Brody[28] introduced steady-state creep deformations into their analysis of the thermal stresses and Heinlein *et al.*[29] proposed a boundary-element method to

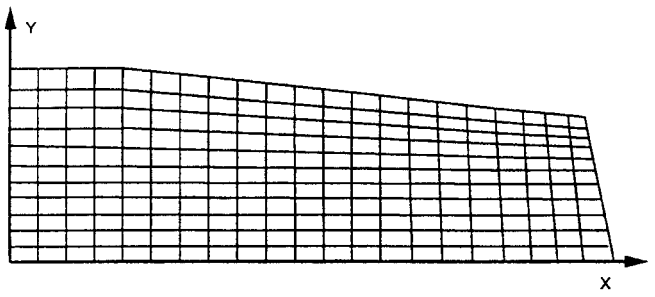

Fig. 2—Finite element enmeshment of a layer of the casting, as viewed from the top.

study transient temperature fields and associated stress fields in static solidifying bodies. Brody *et al.*[30] emphasized the need for accurate mechanical properties of partially solidified alloys in order to predict correctly hot tearing of round aluminum ingots. The most comprehensive modeling work concerning thermomechanical effects during DC casting of aluminum billets has been carried out by Fjaer and Mo.[31] These authors developed the finite-element model Alspen, in which the thermally induced strains and stresses that develop during the casting process were calculated while taking viscoplasticity into account. Smelser and Richmond[32] were the first to use an internal state variable constitutive model previously developed by Sample and Lalli[33] for the computation of the air-gap formation at the casting-mold interface of a solidifying cylindrical piece.

It is surprising that in the previous models of DC or EM casting, little attention has been paid to the nonuniform distortions of the ingot cross section in the steady-state regime. Indeed, it would be very useful to design molds capable of producing nearly flat rolling slabs using numerical methods rather than costly trial-and-errors experiments. At the same time, no investigation of the relative importance of the elastic and creep deformation components in the final ingot distortions has been carried out. The goal of this article is to present a general three-dimensional (3-D) model of the thermomechanical distortions experienced by a DC cast ingot and to elucidate the respective roles of the elastic and creep mechanisms. Particular attention has been paid to the determination of the thermophysical and thermomechanical properties of a commercial aluminum alloy in the solid and mushy states as well as to the estimation of the thermal boundary conditions encountered in the DC casting process. Section II of this article presents a 3-D viscoplastic model of the DC casting of aluminum alloys. The boundary conditions are defined in Section III and the thermophysical and thermomechanical properties used for the calculations are described in Sections IV and V, respectively. Section VI presents the numerical procedure and computed results such as butt curl, butt swell, and steady-state ingot cross section are compared with measured ingot distortions in Section VII. Finally, the main outcomes of such a model are discussed in Section VIII.

II. MODEL FORMULATION

The present model calculates the temperature distribution and the associated thermal stresses in a rolling sheet ingot during the DC casting process and the subsequent cooling of the ingot in the pit. The thermal stresses are partially relieved by viscoplastic mechanisms, and accordingly, the final ingot distortion is expected to be larger than that of a purely elastic metal. Transient thermomechanical computations are carried out on a variable domain from the start phase of casting up to the pseudo–steady-state regime. Thus, the butt curl, the butt swell, the inward rolling faces pull-in, and the final ingot cross section associated with a given mold design are calculated.

A. *Computation Domain*

The computation domain, as viewed from the ingot center in Figure 1, represents one-quarter of the slab, since the two planes (xz) and (yz) are planes of symmetry. The bottom block and the mold are not part of the model and are thus assumed to have a constant shape. The finite-element mesh is made of layers, 2 cm in thickness; each layer fits the exact design of the mold as shown in Figure 2, which represents a top view of the initial ingot shape. The coordinate system is fixed with respect to the slab and the incoming flow of liquid metal is modeled through the activation of successive layers of the enmeshment. The rate at which new layers are introduced corresponds to the casting speed and the lateral cooling conditions are translated along the external faces of the slab according to the casting speed.

B. *Thermal Aspects*

Leaving aside convection in the molten pool, the thermal evolution within the slab is predicted by solving the following heat-conduction equation:

$$\rho C_p^s \partial T/\partial t - \text{div}\ (\kappa \cdot \text{grad}\ T) = 0 \qquad [1]$$

where κ is the thermal conductivity, ρ is the density, and T is the temperature field. The term C_p^s is the equivalent specific heat, which accounts for the latent heat released during solidification.

C. *Mechanical Aspects*

Under the assumption of instantaneous equilibrium, the variation of the internal stress tensor, $\delta\underline{\sigma}$, during a time interval, δt, is obtained in terms of the external force-field variation, $\delta\underline{f}$ (in this case gravity), by solving the following incremental equation:

$$\text{div}\ \delta\underline{\sigma} + \delta\underline{f} = 0 \qquad [2]$$

The incremental deformation tensor $\delta\underline{\varepsilon}$ is assumed to be a superposition of elastic, thermal, and viscoplastic components $\delta\underline{\varepsilon}_e$, $\delta\underline{\varepsilon}_{th}$, and $\delta\underline{\varepsilon}_{vp}$:

$$\delta\underline{\varepsilon} = \delta\underline{\varepsilon}_e + \delta\underline{\varepsilon}_{th} + \delta\underline{\varepsilon}_{vp} \qquad [3]$$

The elastic deformations are related to the internal stresses by Hooke's law:

$$\delta\underline{\sigma} = [\text{D}] \cdot \delta\underline{\varepsilon}_e \qquad [4]$$

where $[D]$ is the stiffness matrix defined in terms of the Young and Poisson modules, E and ν. The thermal deformations are related to the local temperature variation, δT, through the following equation:

$$\delta\varepsilon_{ij} = \alpha \cdot \delta T \cdot \delta_{ij} \qquad [5]$$

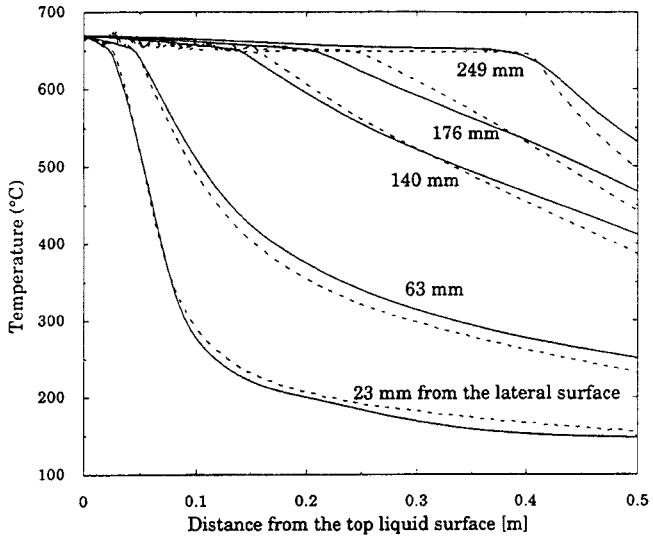

Fig. 3—Measured (dashed lines) and calculated (continuous lines) temperature profiles along five vertical lines within an AA1201 ingot DC cast at 60 mm/min.

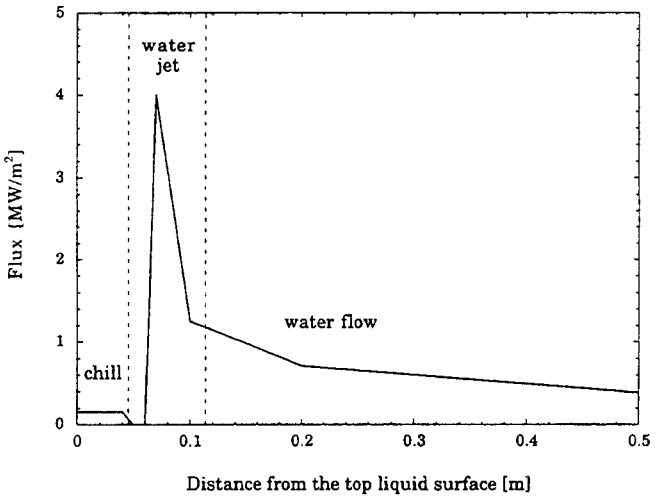

Fig. 4—Height-dependent heat flux as calculated by inverse modeling using the measured temperature profiles shown in Fig. 3.

where α is the linear expansion coefficient and δ_{ij} is the Kronecker symbol.

In addition to the elastic and thermal strains, the present model accounts for the time- and temperature-dependent creep-flow behavior of aluminum.[34] This has an important influence on stress generation at the elevated temperatures and low strain rates encountered during casting processes.[34,35] The strains generated by creep are physically indistinguishable from those resulting from quasi–time-independent plastic flow, particularly at elevated temperatures.[35] Therefore, the plastic and creep deformations are treated in an unified manner *via* a "plastic-creep" strain rate. The time dependence of the viscoplastic deformations usually shows three distinct stages: a primary creep phase during which the creep rate rapidly decreases, a secondary phase with a nearly constant creep rate, and finally the stage just before rupture.[36] At high temperature, the primary stage is neglected and the viscoplastic incremental deformation of the solid is assumed to be given by the following:

$$\delta\underline{\varepsilon}_{vp} = \frac{3}{2} \cdot (\dot{\varepsilon}_{vp} \cdot \delta t) \cdot \underline{\sigma}_d/\sigma_{vm} \qquad [6]$$

where σ_{vm} is the equivalent Von Mises stress, $\underline{\sigma}_d = \underline{\sigma} - tr(\underline{\sigma}) \cdot \underline{Id}/3$ is the deviatoric stress tensor, and $\dot{\varepsilon}_{vp}$ is the isotropic viscoplastic strain rate of the material defined in Section V.

III. BOUNDARY CONDITIONS

Except for the origin of the ingot (Figure 1), which is fixed so as to give enough rigidity to the system, the points located on the two planes of symmetry (xz) and (yz) are free to slide in their respective planes. From a thermal point of view, these two planes are adiabatic for symmetry reasons.

A. *Heat Transfer through the Bottom Block*

Since 3-D transient computations are very intensive, the present investigation does not consider the bottom block and the associated time-dependent heat transfer with the ingot.[25] The thermal flux through the interface between the ingot and the bottom block is assumed to obey a Cauchy-type law. The sink temperature, which is in this case the mean bottom-block surface temperature, was set to 100 °C, whereas the heat-transfer coefficient, h, was chosen to be a decreasing function of the vertical displacement of the ingot so as to give a butt curl during the starting phase that was close to the experimental result (Section VII).

B. *Primary and Secondary Coolings*

The thermal boundary conditions associated with the lateral cooling of the ingot by the water spraying were accurately determined using inverse modeling. The estimation of the space-dependent lateral heat flow is described in Reference 37 and is briefly reported here. After a nearly steady-state regime was obtained, five thermocouples were immersed from the top of the melt pool at various distances from the lateral surface of the ingot in the midplane of a DC cast aluminum slab.[7] Since the thermocouples were attached to two long rods already trapped by the solid part of the ingot, they were translated at the same speed as the withdrawal rate of the ingot. After the measurement, the cooling curves measured at each thermocouple location were converted into temperature profiles along the height of the casting (stationary situation). These profiles are displayed with dashed lines in Figure 3 for the AA1201 aluminum alloy.

With the help of the software 3-MOS,[37] these temperature profiles were then used to deduce by inverse modeling the height-dependent heat flow extracted at the lateral surface of the ingot by the chill and by the water-spraying system underneath. The results are shown in Figure 4 as a function of the distance from the top free liquid surface. As can be seen, a heat flow of a few hundreds kW/m² is extracted from the ingot during the initial contact with the chill but the heat flow almost vanishes as soon as an air gap forms. At the location of the water-spraying impingement, the heat flow is maximum (nearly 4 MW/m²). It decreases then to lower values as water flows and evaporates along the side of the ingot. The temperature profiles calculated with the boundary conditions of Figure 4 are also

Table I. Thermophysical Properties of the AA1201 Alloy (As Used in the Computations)

T(°C)	κ(W/mK)	C_p(kJ/kg·K)
27	227	0.905
127	230	0.950
227	227	0.998
327	222	1.043
427	216	1.090
527	210	1.135
630 (solidus)	203	1.181
658 (liquidus)	90*	1.086

*This value is increased to 300 W/mK to take into account liquid convection in the sump. ρ = 2650 kg/m³; L = 9.5 10^8 J/m³.

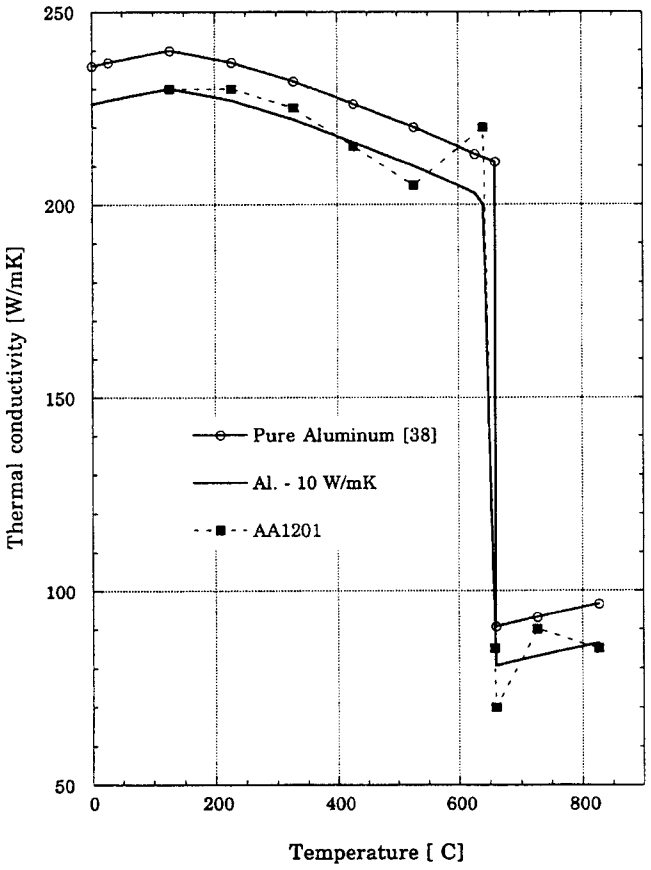

Fig. 5—Temperature-dependent thermal conductivity of the AA1201 alloy as deduced from inverse modeling and compared with values of pure aluminum.[38]

shown in Figure 3 with solid lines. As can be seen, the agreement with the measurements (dashed lines) is quite good. The calculated height-dependent heat flow is applied on the lateral surfaces of the slab with the help of a heat-transfer coefficient depending on the position and a constant water temperature of 10 °C.

C. *Upper Moving Boundary*

The upper moving boundary of the domain corresponds to the incoming flow of liquid metal through the activation of successive layers of the enmeshment. The temperature of the new volume elements is set to that of the incoming metal, 670 °C.

IV. THERMOPHYSICAL PROPERTIES

The industrial alloy AA1201 is a commercial-purity aluminum alloy and its exact composition is given in Reference 7. This alloy was DC cast and the ingot distortions were measured,[7] thus allowing a comparison with the simulation results. Furthermore, the slabs were cut and as-cast samples were machined in order to perform subsequent material testings. Thermophysical properties used for the following calculations are defined in Table I and some of them are discussed hereafter.

A. *Specific and Latent Heat*

The AA1201 alloy investigated here contains only small amounts of iron and silicon. Therefore, its specific heat, C_p, and latent heat, L, have to be close to the values characterizing pure aluminum. The values that have been used in the numerical simulations that follow are taken from Reference 38 and are given in Table I. The liquidus, T_l, and solidus, T_s, temperatures of this alloy are 658 °C and 630 °C, respectively.[39] Even though most of the latent heat is released near the liquidus for such an alloy (*i.e.*, solidification path given by a Scheil–Gulliver approximation[40]), the volume fraction of solid, f_s, has been assumed to be linear between these two temperatures for a faster convergence of the computations. It has been checked that this assumption had no influence on the final stress-strain results. In the mushy zone, the specific heat has been averaged over the solid and liquid phases. Thus, the equivalent specific heat was given by the following:

$$\rho C_p^e = \rho C_p^s f_s + \rho C_p^l (1 - f_s) + \frac{L}{T_l - T_s} [u(T_l - T) - u(T_s - T)] \quad [7]$$

where u is the Heaviside function (the indices s and l refer to the solid and liquid, respectively).

B. *Thermal Conductivity*

Contrary to the specific heat, the thermal conductivity of aluminum alloys is highly dependent on the alloying elements or impurities, even at low concentration. Thus, special attention has been paid to the exact knowledge of the temperature-dependent thermal conductivity. Again, inverse modeling was used for this purpose.[37] Cylindrical castings of the AA1201 aluminum alloy were solidified under one-dimensional heat-flow conditions. The details of this experimental setup are given in Reference 41. Once a uniform temperature was reached, the furnace was removed and an instrumented water-cooled copper chill was applied to the bottom surface of the mold, which consisted of a thin high-conductivity aluminum nitride plate. Seven thermocouples were placed at various heights of the aluminum ingots. The first thermocouple near the chill was taken as a boundary condition, to determine by an inverse calculation the temperature-dependent thermal conductivity of the aluminum alloys using the six remaining cooling curves. The result of such an inverse calculation is shown in Figure 5 for the alloy AA1201. The thermal conductivity of pure aluminum[38] is given for comparison. As can be seen, the inverse modeling calculation gives a thermal conductivity that follows that of the pure material, but about 10 W/mK below,

Table II. Thermomechanical Properties of the AA1201 Alloy (As Used in the Computations)

T(°C)	E (GPa)	α (10^{-6}/K)
25	68.2	23.2
200	60.6	25.2
400	51.8	30.23
630 (solidus)	41.8	34.3
650 (coherency)	40	38.4
650.1	0.1	0.0
658 (liquidus)	0.1	0.0

ν = 0.37.

both in the solid and liquid phases. A small oscillation of the thermal conductivity is observed near the phase transition. This is attributed to the way the equivalent specific heat is calculated.

Despite the low thermal conductivity deduced for the liquid (80 to 90 W/mK), the value of the thermal conductivity in this phase was increased to a larger value in the numerical computations (400 W/mK) so as to account for liquid convection in the sump. This value was determined by calculating the steady-state sump depth in the plane of symmetry (yz) and by comparing the result with the measured value.[7] The influence of convection on thermomechanical effects mainly occurs *via* the thermal exchanges: variation of the dynamic pressure in the liquid is orders of magnitude smaller than the stresses and the metallostatic pressure is already accounted for *via* the gravity term in Eq. [2].

V. THERMOMECHANICAL PROPERTIES

The computation domain includes the liquid metal, the mushy zone, and the solid part. The density of the metal is supposed to be constant. The liquid metal is assumed to be incompressible and fluid motion is neglected (except for the increased thermal conductivity introduced for the liquid phase). Above a certain temperature, called the coherency temperature, T_c, the alloy is treated like a liquid, and below T_c, it is treated like a solid.[42] The coherency temperature is the temperature at which the dendrites form a coherent network that develops some strength, thus resulting in a behavior close to that of a solid. Above this temperature, the grains are free to move and the solid-liquid mixture is treated rather like a liquid. The contribution of the metal shrinkage during solidification is neglected as a result of the constant liquid feeding within the mushy zone.[7] The alloy is allowed to contract as soon as it reaches its coherency temperature. The determination of T_c is detailed hereafter. The thermomechanical properties of the AA1201 alloy are presented in Tables II through IV and are discussed further.

A. *Elastic Moduli and Linear Thermal Expansion Coefficient*

The temperature dependence of the Young modulus, E, and of the dilatation coefficient is taken into account and the values of these parameters are assumed to be equal to that of pure aluminum.[29] The differential temperature-dependent coefficient of linear thermal expansion as found in Reference 29 was transformed into a mean coefficient, taking as the reference temperature the coherency temperature of the alloy. The Young modulus rapidly decreases from its value of 40 GPa to a very low value, 0.1 GPa, above the coherency temperature. These values are listed in Table II, whereas the Poisson modulus, ν, was assumed to be constant.

Table III. Parameters for the Creep Behavior in the Solid State (As Used for the Computations)

	A(s^{-1})	Q(kJ/mol)	n(—)	σ_0(MPa)
AA1201	$28.2 \cdot 10^{25}$	400.0	7.13	13.6

Table IV. Parameters for the AA1201 Creep Behavior in the Mushy State (As Used for the Computations)

T(°C)	k(s^{-1})	n(—)	σ_0(MPa)
635.0	2.1×10^{-6}	4.76	1.0
640.0	6.9×10^{-6}	3.85	1.0
645.0	1.36×10^{-4}	3.5	1.0
650.0	1.15×10^{-3}	3.4	1.0

B. *Viscoplastic Behavior in the Solid State*

Creep data of aluminum alloys, if available, are usually determined for cold or hot rolling/extrusion or for the calculation of component deformation. Furthermore, subsequent heat treatment or recrystallization can be applied to the cast metal. Therefore, for the present investigation, it was necessary to obtain such data over a wide range of temperatures (from room temperature up to the coherency temperature) and, more importantly, for alloys having the as-cast microstructure. From the DC cast aluminum alloy AA1201, standard creep specimens with 40-mm gage length and 8-mm diameter were machined and tested at constant load in high-resolution creep machines at temperatures ranging from 300 °C to the solidus temperature. The test temperature was reached as fast as possible in order to prevent any major change in the as-cast microstructure. The results of these measurements are reported in Reference 43. The measured minimum creep rates at different temperatures and loads were fitted using the Garafalo law:[44]

$$\dot{\varepsilon}_{vp} = A(\sinh(\sigma_{vm}/\sigma_0))^n \exp(-Q/RT) \qquad [8]$$

where A, σ_0, and n are some alloy-dependent constants, Q represents the apparent creep activation energy, and R and T are the universal gas constant and temperature, respectively. After determining the apparent creep activation energy,[43] the remaining constants A, n, and σ_0 were calculated by representing the temperature-compensated Zener–Hollomon parameter, $\dot{\varepsilon}_{vp} \cdot \exp(Q/RT)$, as a function of stress and by fitting this curve by a hyperbolic sine function. Figure 6 shows the resulting curve fitting and Table III gives the value of the parameters.

C. *Mechanical Behavior of the Semisolid State*

Although the mechanical behavior of semisolid alloys is of great importance for the modeling of thermomechanical stresses and hot tearing during casting, it is usually poorly known. Some interesting experiments have been designed by Ackerman and Kurz.[45] In the present case, the mechan-

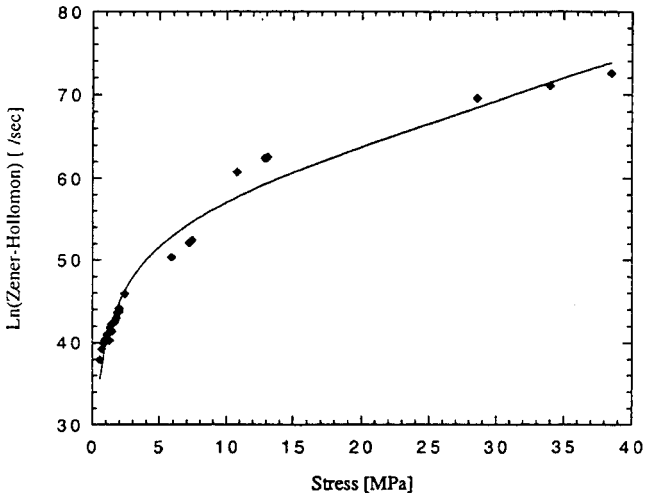

Fig. 6—Zener–Hollomon parameter as a function of stress for the alloy AA1201.

ical behavior of the AA1201 alloy in the semisolid state was investigated using a simple indentation test capable of reproducing the typical strain rates encountered in solidification processes (10^{-4} to 10^{-1} s^{-1}). The measured resistance was then interpreted in terms of a viscoplastic law (inverse method) using a finite-element code. The details of this new approach, known as "computer-assisted rheology," are described in References 46 and 47. The as-cast sample, which was heated to a given temperature, was indented by a 3-mm-diameter needle that was pushed at a constant rate into the metal. The basic assumption is that the semisolid behavior of the metal can be described by a viscoplastic Norton–Hoff law:

$$\dot{\varepsilon}_{vp} = k_i \cdot (\sigma_{vm}/\sigma_{0i})^{n_i} \quad [9]$$

where k_i, σ_{0i}, and n_i are temperature-dependent parameters. These parameters were fitted by comparing the result of the finite-element method (FEM) code with the measured force-displacement curve. Experimental curves obtained for the AA1201 alloy at 635 °C, *i.e.*, 5 °C above the solidus temperature, are presented in Figure 7 for three different indentation speeds. The viscoplastic law was determined at four different temperatures and the corresponding parameters are given in Table IV. For the numerical analysis, the strain rate was interpolated in between the measured values. The coherency temperature was determined as follows. Above this temperature, the force-displacement curves of the needle present many fluctuations and their shape is totally different from the simulation result. Below this temperature, the experimental curve is fairly smooth (Figure 7) and agrees with the numerical result. For the alloy AA1201, the coherency temperature was found to be 650 °C, for which the corresponding solid fraction was estimated to be 40 pct.[39]

VI. NUMERICAL PROCEDURE

The finite-element program ABAQUS has been employed to perform the numerical computations. The fully coupled simultaneous heat-transfer and stress analysis was performed using 8-node brick elements with trilinear displacement and temperature interpolations. This code allows

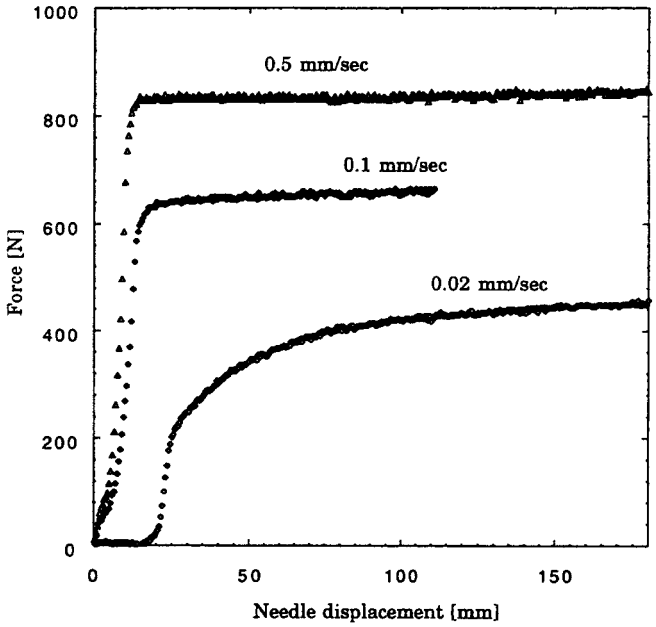

Fig. 7—Force as a function of needle displacement measured at 635 °C during the indentation test.

the user to specify complex viscoplastic behavior of materials and flexible boundary conditions through user subroutines.[48] Successive layers of elements can be added to simulate the evolution of the casting shape. The nonlinearities introduced by the material properties (creep and latent heat) are treated by a Newton–Raphson integration scheme: at each time-step, iterations, with an updating of the material characteristics, are made until both thermal and mechanical equilibrium are reached within the tolerances set by the user. The accuracy parameters were set as the maximum difference in the creep strain increment calculated from conditions at the beginning and at the end of the increment, and the maximum temperature change within the increment. An implicit integration scheme was used, but the typical time-step remained of the order of 0.1 seconds and required typically three iterations before convergence was achieved within each step. The resulting computation time was about 7 days on an HP*-735 workstation for a 3-D domain including 8000 nodes and 6000 elements. For two-dimensional (2-D) geometries, the computation time decreased to 1 day for a domain including 1300 nodes and 1200 elements.

*HP is a trademark of Hewlett-Packard Company, Colorado Springs, CO.

VII. RESULTS

In this section, the results of the temperature and deformation field computations are presented and compared with the measurements of ingot distortions previously made and described in Reference 7. The computations refer to the DC casting of the alloy AA1201 at 60 mm/min, the nominal ingot cross section being 1860 by 510 mm. The calculations were performed until a pseudo steady state was reached, from both a thermal and a mechanical point of view. In order to obtain such conditions, it was found that a cast

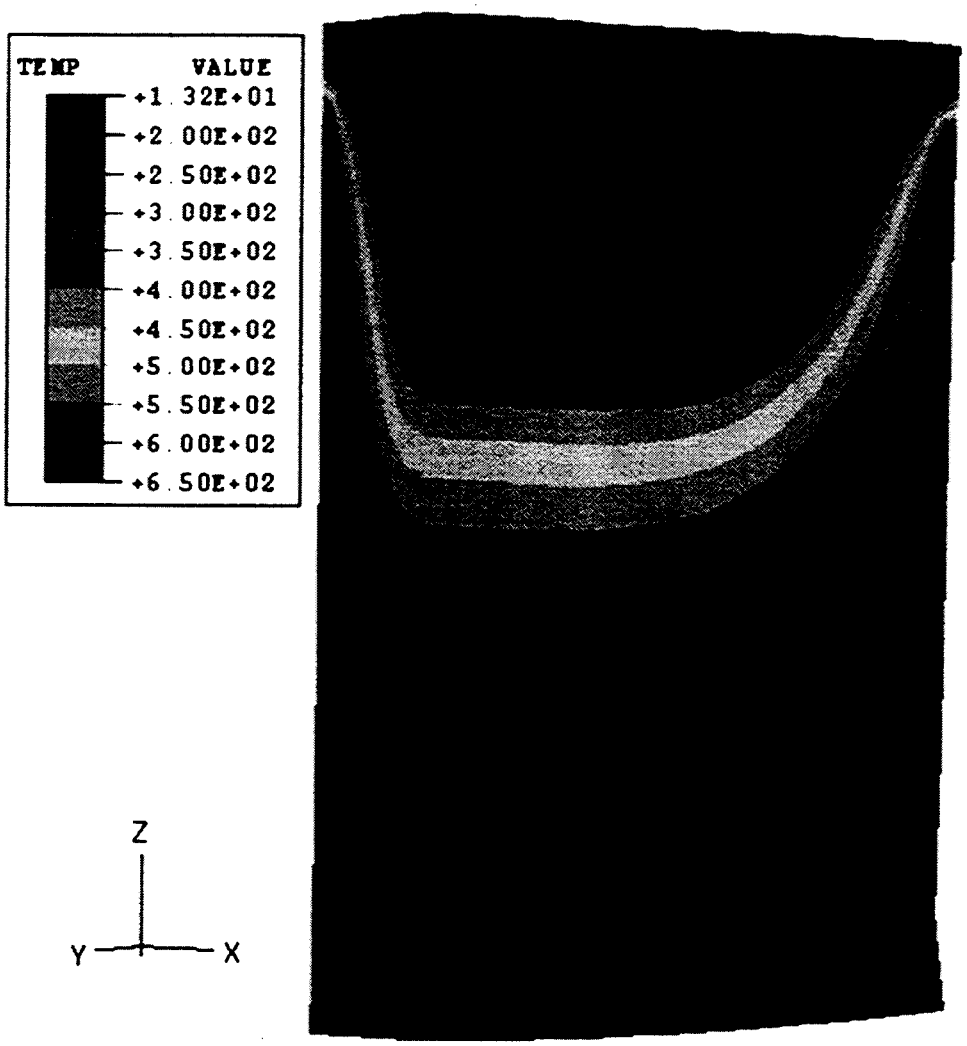

Fig. 8—Computed steady-state temperature profile inside the casting as viewed from the center (AA1201 DC cast at 60 mm/min).

length of about 1.5 m had to be modeled. In the interest of accuracy, the results presented here are for 2.5-m final length castings.

A. *Butt Curl*

Figure 8 shows the computed steady-state temperature profile after a cast length of 1.5 m as viewed from the center. Below the exit point of the mold, the temperature at the periphery of the ingot is lower than 200 °C, thus giving enough strength to the solid shell to support the liquid pool. The sump depth is approximately 60 cm, a value that agrees well with the measurements performed in Reference 7. Assuming that the bottom block is totally rigid, the vertical displacement of the metal represents the width of the air gap that forms between the starting block and the ingot. For the present calculations, the local heat-transfer coefficient was a decreasing function of the air-gap width: this coefficient decreases from a value of 2000 W/m²K when the gap, *i.e.*, the vertical displacement of the metal, was lower than 0.1 mm to a value of 200 W/m²K when the gap was larger than 1 mm. Figure 9 presents the calculated vertical displacement of the point at the extreme corner of the lower face of the slab as a function of time. As soon as the cooling water impinges the ingot, the butt rises rapidly, thus generating a large air gap between the metal and the starting block. Consequently, the heat extraction rapidly falls to its low value and provokes a reheating of the butt.

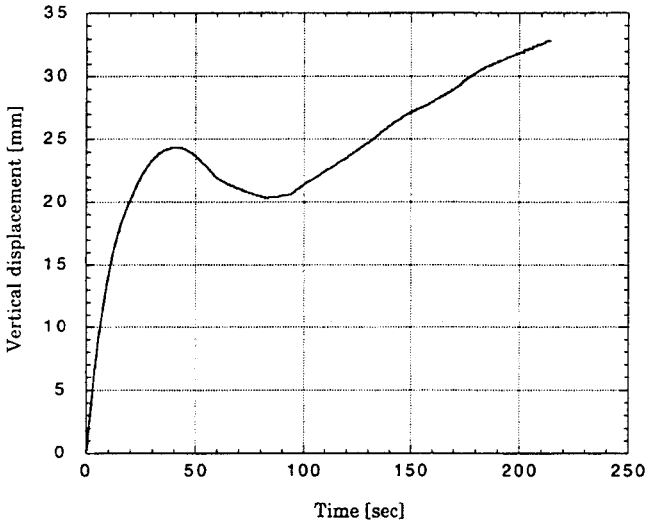

Fig. 9—Computed vertical displacement of the ingot corner as a function of time (the origin of time corresponds to the first chilling by the cooling water on the ingot).

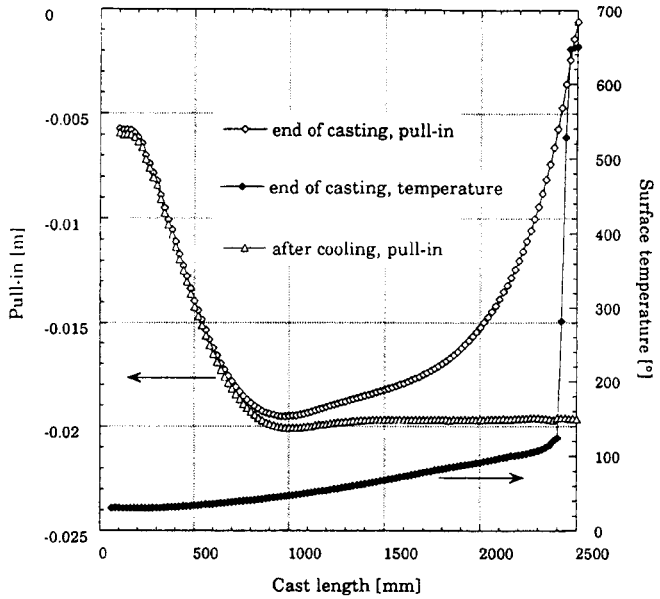

Fig. 10—Calculated rolling faces pull-in and ingot surface temperature as a function of the cast length at the end of casting and after complete cooling.

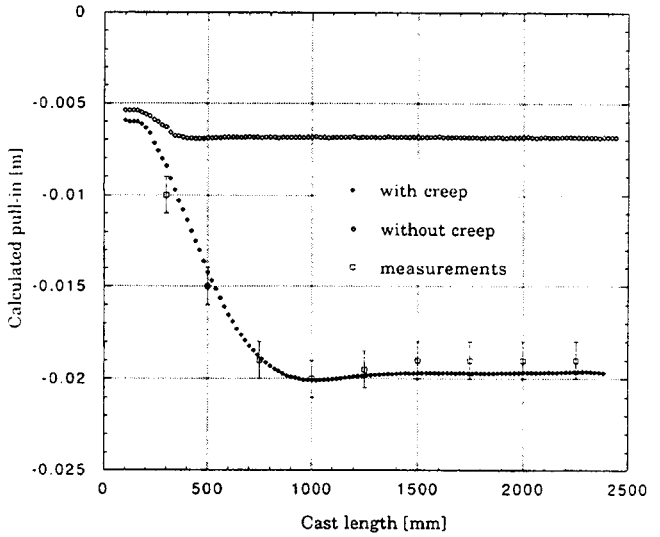

Fig. 11—Computed ingot pull-in with and without creep deformation compared to the measurements.

Table V. Value of the *cps* Parameter Close to the Axis and Near the Ingot Surface at Different Temperatures

Temperature	Center	Surface
650 °C	0 pct	0 pct
630 °C	0.33 pct	0.023 pct
20 °C	2.19 pct	2.33 pct
$\frac{cps(t_{630}^*)}{cps(t_{20}^*)}$	15 pct	1 pct

$^*t_{630}^*$ and t_{20}^* are times for the metal to reach a temperature of 630 °C and 20 °C, respectively.

which can therefore relax more easily the thermal stresses. The ingot butt then falls a few millimeters before rising again after 90 seconds in Figure 9.

B. *Rolling Faces Pull-In*

The thermal field presented in Figure 8 clearly shows that the temperature profile in the plane (*yz*) remains unchanged along a certain distance in the *x* direction. Consequently, a 2-D calculation of the ingot rolling faces pull-in can be performed in the plane (*yz*) (Figure 1) under the assumption of planar deformation and 2-D heat flow. Figure 10 reports the ingot surface temperature and the contraction profile just at the end of casting, *i.e.*, as the metal feeding is stopped, as obtained with this 2-D model. The rolling faces pull-in is also presented after a cooling period of 1 hour on the same figure. This clearly demonstrates that a stationary regime had been reached, leading to a constant pull-in of about 20 mm for the half-thickness of the slab. The calculated and measured ingot profiles along the *z* direction after cooling are compared in Figure 11. The final ingot profile was also computed under the assumption of only thermoelastic deformation of the metal, *i.e.*, $\dot{\varepsilon}_{vp} = 0$ (open diamonds in Figure 11). In order to assess the relative importance of the plastic deformation in the mushy zone, *i.e.*, between the coherency and solidus temperatures, the cumulated plastic strain, *cps*(*t*), has been computed. This quantity is defined as follows:

$$cps(t) = \int_0^t \sqrt{\frac{2}{3} d\varepsilon_{vp} : d\varepsilon_{vp}} \qquad [10]$$

where $d\varepsilon_{vp}$ is the increment of viscoplastic strain at time *t*. This parameter was calculated during the steady-state regime of casting at two integration points, one near the vertical axis of the slab and one close to the ingot surface. The value of this quantity at the coherency, solidus, and room temperatures is reported in Table V.

C. *Ingot Cross Section and Influence of the Mold Design*

In order to investigate the effect of the mold shape on the resulting slab cross section, it is necessary to perform 3-D computations so as to take into account the edge reinforcement.[7] The computed and measured steady-state ingot cross section of the AA1201 alloy after complete cooling are compared in Figure 12 for two different casting speeds, 60 and 80 mm/min. Also shown in this figure are the interior mold shape and the desired half-ingot thickness, which is very close to the final thickness of the short sides. The measured nonuniform ingot contraction and the effect of increased casting speed are well reproduced by the present model. After this validation of the model, different mold designs were studied: one with no central segment (mold A), one with a small central segment (mold B), and one with a large central segment (mold C). The computed final ingot cross sections obtained for these three different mold shapes are reported in Figure 13, together with the corresponding mold designs. The inward pull-in of the center of the rolling faces and the contraction of the short sides remain constant irrespective of the mold design and correspond to the values calculated by the 2-D model (Figure 12).

VIII. DISCUSSION

In the light of their experimental investigation, Drezet *et al.*[7] have explained qualitatively the ingot distortion oc-

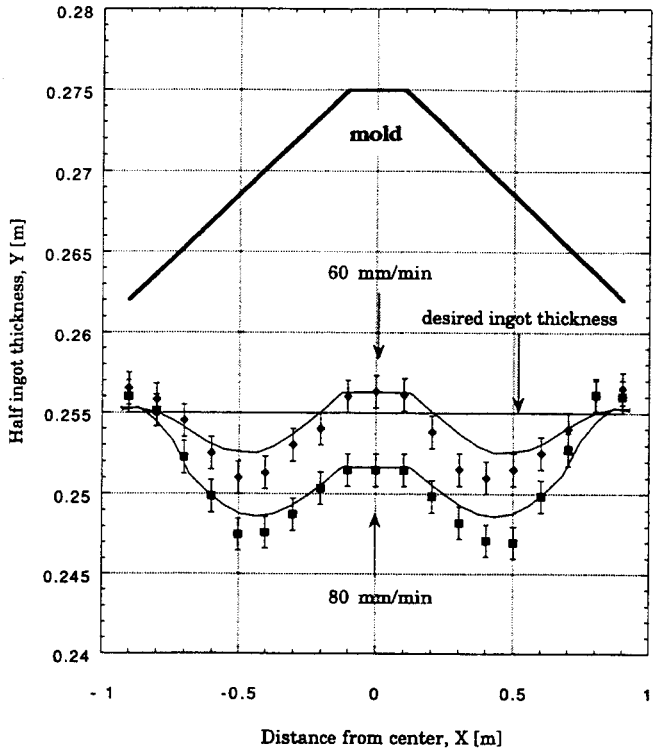

Fig. 12—Computed and measured steady-state ingot cross section for the alloy AA1201 cast at 60 and 80 mm/min.

curring during DC casting of aluminum alloys in terms of liquid pool extension, bending of the solid shell, and associated cumulated deformation with the help of a simple thermoelastic model. Neglecting the plastic deformation, they underestimated the deformation of the ingot and at the same time overestimated the stresses. Furthermore, they considered neither the movement nor the evolution of the solid domain, whereas the present finite-element model takes into account the plastic flow of the metal and is therefore quantitatively much closer to reality in computing the final ingot cross section. Nevertheless, the main conclusion regarding the mechanisms responsible for the large and nonuniform rolling faces pull-in remain the same: a 9 pct pull-in of the rolling faces does not correspond to a 9 pct deformation since bending (and shearing) of the solid shell occurs.

A. *Nonuniform Contraction of the Metal during Casting*

During solidification of a metal, there are essentially two contributions to the ingot contraction: the first one is associated with the phase change (about 6.5 pct in volume for aluminum[49]) and the second contribution arises from the solid-state thermal contraction during subsequent cooling (about 2 pct in linear contraction, *i.e.*, about 6 pct in volume). In the DC casting process, there is a constant liquid feeding within the mushy zone to compensate for the density variation through the liquid-to-solid phase transformation, thus eliminating the first contribution to explain the large contraction of the slab. The pull-in measured at the ingot center during DC casting (Figures 12 and 13) after complete cooling is therefore a consequence of the deformation of the solid ingot.

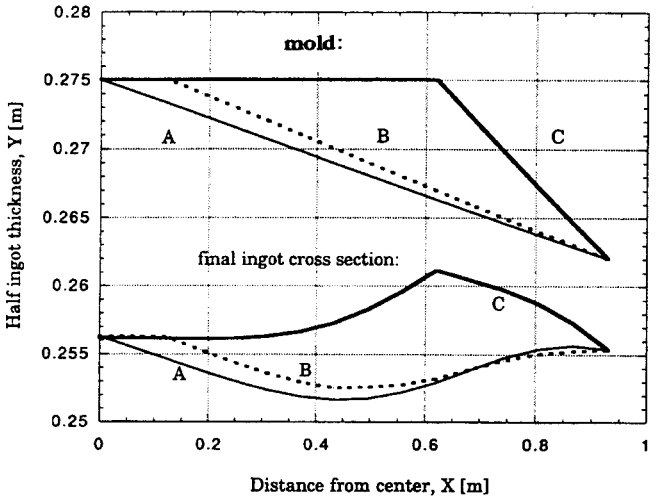

Fig. 13—Computed steady-state ingot cross section for three mold designs (alloy AA1201 cast at 60 mm/min).

B. *Inward Pull-In of the Rolling Faces*

The thermal conditions associated with DC casting lead to the appearance of a thin solid shell in between the two cooling zones and nearly parallel to the mold. This thin shell contracts under the high local thermal gradient (Figure 10), the metallostatic pressure being negligible. However, as shown in Figure 10, the last solid to have formed at the end of the casting has about the size fixed by the mold opening (*i.e.*, contraction equals zero at 2.5 m when this part has just solidified). After cooling to room temperature, each lateral face of the ingot experiences a 20-mm pull-in. Although thermal contraction is only 2 pct for a uniform-temperature specimen and would represent 5.5 mm in this case, the *bending* and associated *cumulated deformation* of the solid shells during continuous casting explain this large pull-in. It should be emphasized that this pull-in is a relative displacement, in this case a contraction, and must not be considered as a mechanical deformation.

As the casting speed is increased, the liquid pool becomes deeper and the thermal gradient at the level of the cooling water jet is more horizontal. As a result, the amplitude of bending is larger and the pull-in increases to reach a value of 24 mm, *i.e.*, 9 pct in contraction, for a casting drop of 80 mm/min (Figure 12). Near the short sides of the ingot, the sump may have about the same shape as along the rolling faces, but it is now turned 90 deg (Figure 8). Consequently, inward bending of the solid shells is no longer possible and the metal contraction along the y direction corresponds mainly to the thermoelastic contraction, about 7 mm, calculated and reported in Figure 11. Eventually, the contraction of the short sides is almost unaffected by the casting speed (Figure 12).

C. *Boundary Conditions and Material Parameters*

The thermal boundary conditions applied in this model play a key role as they dictate the shape and extension of the sump, thus influencing the bending of the solid shell and the resulting ingot cross section.

The mechanical behavior of the solid metal determines to a large extent the degree of bending of the solid shells under the high thermal gradients and mainly dictates the

butt curl. It has been described in the present model by a general function linking the strain rate, the temperature, and the stress (Eq. [8]). The use of such a function is motivated by the fact that it is simple to implement such a relation in a subroutine defining the plastic behavior of the metal. An apparent creep activation energy of 400 kJ/mole was determined for the as-cast microstructure, which is larger than the activation energy of aluminum lattice diffusion, 142 kJ/mole.[50] The stress exponent is also larger than typical values found for pure aluminum.[50] As explained by Frost and Ashby,[50] discrete obstacles like dispersions, forest dislocations, and solute elements limit the velocity of dislocations: the activation energy of this obstacle-controlled glide is much larger than the self-diffusion activation energy.

As shown in Table V, 15 pct of the plastic straining occurs in the mushy zone near the axis of the ingot, and only 1 pct occurs near the surface. The mushy zone is larger along the axis of the slab, thus allowing more time for the metal to relax thermal stresses through creep deformation. On the other hand, the chilling of the ingot surface is so rapid that almost no plastic deformation occurs.

D. *Process Optimization*

The calculated vertical displacement of the ingot butt (Figure 9) agrees well with the measurements performed by Carrupt and Moulin[6] and Krähenbühl *et al.*[24] Although the coupling between thermal and mechanical effects is particularly strong during the start phase of the process, the use of a decreasing heat-transfer coefficient leads to a reasonable description of the butt-curl phenomenon. The butt-curl speed, *i.e.*, the time derivative of the vertical displacement of the ingot butt, is very high just after the cooling water had impinged the ingot. The model presented here seems suitable and promising in optimizing the cooling system and also in choosing the appropriate bottom-block geometry and casting parameters during the nonstationary starting phase of the DC casting process. Moreover, special attention has to be paid to the stress generation, especially the σ_{xx} component, which may lead to the initiation of longitudinal cracks.

Eventually, considerable amount of cast metal could be saved by reducing the scalping thickness of the ingot before rolling. The present thermomechanical model has been validated using ingot cross-section measurements carried out in the steady-state regime of casting (Figure 12). The numerical investigation of molds A and C revealed that neither of these two molds is capable of producing flat rolling sheet ingots. The use of straight line segments seems oversimplistic for this aim. In the light of these computations, it has been made clear that the 3-D extension of the liquid pool in the steady-state regime of casting has a great influence in the inward rolling faces pull-in.

IX. CONCLUSIONS

The 3-D thermomechanical model presented here has been validated using ingot distortion measurements. This model is able to predict with accuracy the butt curl of the ingot during the starting phase and the transient and steady-state rolling faces pull-in as a function of the casting conditions (casting speed, ingot size, and mold shape). The input data, thermophysical and thermomechanical properties as well as boundary conditions, have been paid particular attention because the final ingot shape is the result of several interplaying phenomena. With the help of this model, it is shown that a nearly steady-state thermomechanical regime is reached after about 1-m cast length. The horizontal component of the thermal gradient during the stationary casting regime provokes an inward bending of the solid shell and is therefore responsible for the large rolling faces pull-in measured at the center of the ingot. The 3-D nature of the liquid pool explains why the contraction of the short sides corresponds only to a thermal contraction. The optimization of the mold bow and of the casting conditions, diminishing butt sawing and cracking initiation during the starting phase and ingot scalping, could save development time and cost by avoiding the empirical method of mold design. The simulation of the DC casting process, as described in the present model, appears to be a promising tool in achieving this task.

ACKNOWLEDGMENTS

This research has been funded by the Commission pour l'Encouragement de la Recherche Scientifique (Berne), under Grant No. CERS 2365, and by Alusuisse-Lonza Services Ltd. (Chippis). The authors wish to greatly thank Drs. Y. Krähenbühl and B. Carrupt for constructive reading of this article.

REFERENCES

1. E.F. Emley: *Int. Met. Rev.*, 1976, June, pp. 75–115.
2. R.E. Spear and H. Yu: *Aluminum*, 1984, p. 440.
3. Ho Yu: *Light Met.*, 1980, p. 613.
4. W. Droste and W. Schneider: *Light Met.*, 1991, p. 945.
5. *Alusuisse Casthouse Seminar*, Alusuisse–Lonza Services Ltd., Chippis, Switzerland, 1994.
6. B. Carrupt and C. Moulin: *8th Int. Sheet and Plate Conf.*, Louisville, KY, Oct. 5–8, 1993.
7. J.-M. Drezet, M. Rappaz, B. Carrupt, and M. Plata: *Metall. Trans. Mater. B*, 1995, vol. 26B, pp. 821–29.
8. C.H. Weaver: *An Empirical Model to Explain Cross-Section Changes of D.C. Sheet Ingot during Casting*, TMS-AIME, Warrendale, PA, 1976, p. 441.
9. C.H. Weaver: *Light Met.*, 1991, p. 953.
10. O. Richmond: in *Modeling of Casting, Welding and Advanced Solidification Processes*, H.D. Brody and D. Apelian, eds., TMS, Warrendale, PA, 1981, p. 215.
11. N. Zabaras and V.R. Voller: in *Modeling of Casting, Welding and Advanced Solidification Processes*, A.F. Giamei and G.J. Abbaschian, eds., TMS, Warrendale, PA, 1988, vol. 4. p. 683.
12. B.G. Thomas: in *Modeling of Casting, Welding and Advanced Solidification Processes* T.S. Piwonka, V. Voller, and L. Katgerman, eds., TMS, Warrendale, PA, 1993, vol. 6, p. 519.
13. L. Katgerman, S.C. Flood and A.H. Langille: in *Production, Refining, Fabrication and Recycling of Light Metals*, M. Bouchard and P. Tremblay, eds., Pergamon Press, Hamilton, Ontario, vol. 19, 1990, p. 97.
14. O. Richmond and R.H. Tien: *J. Mech. Phys. Solids*, 1971, vol. 19, p. 273.
15. J.O. Kristiansson: *J. Thermal Stresses*, 1982, vol. 5, p. 315.
16. A. Grill and K. Schwerdtfeger: *Ironmaking and Steelmaking*, 1979, vol. 3, p. 131.
17. B.G. Thomas, I.V. Samarasekera, and J.K. Brimacombe: *Metall. Trans. B*, 1987, vol. 18B, pp. 119–30.
18. J.R. Williams, R.W. Lewis, and K. Morgan: *Int. J. Numer. Methods Eng.*, 1979, vol. 14, p. 1.
19. J.E. Kelly, K.P. Michalek, T.G. O'Connor, B.G. Thomas, and J.A. Dantzig: *Metall. Trans. A*, 1988, vol. 19A, pp. 2589–2602.

20. D.C. Weckman and P. Niessen: *Can. Metall. Q.*, 1984, vol. 23, p. 209.
21. B. Hannart, F. Cialti, and R.V. Schalkwijk: *Light Met.*, 1994, p. 879.
22. H.G. Fjaer and E.K. Jensen: *Light Met.*, 1995, p. 951.
23. E.K. Jensen and W. Schneider: *Light Met.*, 1990, p. 937.
24. Y. Krähenbühl, R. Von Kaenel, B. Carrupt, and J.C. Weber: *Light Met.*, 1990, p. 893.
25. S. Mariaux, M. Rappaz, Y. Krähenbühl, and M. Plata: *Light Met.*, 1992, p. 175.
26. J. Moriceau: *Light Met.*, 1975, p. 119.
27. B. Janin: *State of the Art of Computer Simulation of Casting and Solidification Processes*, H. Fredriksson, ed., Les Editions de Physique, Strasbourg, France, 1986, p. 305.
28. J. Mathew and H.D. Brody: *Nucl. Metall.*, 1976, vol. 20 (2), p. 978.
29. M. Heinlein, S. Mukherjee, and O. Richmond: *Acta Mech.*, 1986, vol. 59, p. 59.
30. H.D. Brody, P. Wisniewski, A. Gokhale, and J. Mathew: in *Modeling of Casting, Welding and Advanced Solidification Processes*, A.F. Giamei and G.J. Abbaschian, eds., TMS, Warrendale, PA, 1988, vol. 4, p. 351.
31. H. Fjaer and A. Mo: *Metall. Trans. B*, 1990, vol. 21B, pp. 1049–61.
32. R.E. Smelser and O. Richmond: in *Modeling of Casting, Welding and Advanced Solidification Processes*, A.F. Giamei and G.J. Abbaschian, eds., TMS, Warrendale, PA, 1988, vol. 4, p. 313.
33. V.M. Sample and L.A. Lalli: *Mater. Sci. Technol.*, 1987, vol. 3, p. 28.
34. L. Anand: *Trans. ASME*, 1982, vol. 104, p. 12.
35. A. Mo and E.J. Holm: *J. Thermal Stresses*, 1991, vol. 14, p. 571.
36. *Introduction to Creep*, R.W. Evans and B. Wilshire, eds., The Institute of Materials.
37. M. Rappaz, J.L. Desbiolles, J.M. Drezet, C.A. Gandin, A. Jacot, and P. Thevoz: *Modeling of Casting, Welding and Advanced Solidification Processes*, TMS, Warrendale, PA, 1995, p. 449.
38. R.D. Pehlke, A. Jeyrajan, and H. Wada: *Summary of Thermophysical Properties for Casting Alloys and Mold Materials*, University of Michigan Report, University of Michigan, Ann Arbor, MI, 1982.
39. J.P. Gabathuler: *Thermoanalyse*, Alusuisse Internal Technical Report, June 1985.
40. W. Kurz and D.J. Fisher: *Fundamentals of Solidification*, Trans Tech Publications, Aedermannsdorf, Switzerland, 1984.
41. J. Ampuero, A.F.A. Hoadley, and M. Rappaz: in *Modeling of Casting, Welding and Advanced Solidification Processes*, M. Rappaz, M.R. Ozgu, and K.W. Mahin, eds., TMS, Warrendale, PA, 1991, vol. 5, p. 449.
42. R.J. Claxton: eds., *J. Met.*, 1975, Feb., p. 14.
43. J.M. Drezet and G. Eggeler: *Scripta Metall. Mater.*, 1994, vol. 31, p. 757.
44. F. Garafalo: *Trans. TMS-AIME*, 1963, vol. 227, p. 351.
45. P. Ackermann and W. Kurz: *Mater. Sci. Eng.*, 1975, vol. 75, p. 79.
46. P. Vicente: Ph.D. Thesis, Ecole Nationale Superieure des Mines de Paris, Paris, 1994.
47. O. Branswyck, J. Collot, P. Vicente-Hernandez, A.-M. Chaze, and C. Levaillant: in *Euromat 1991*, J.W. Clyne, ed., Institute of Metals, London, 1992, pp. 124–30.
48. *Abaqus Theory Manual*, K. Hibbit and J. Sorensen, eds., Hibbit, Karlson and Sorensen, Inc., Providence, RI, 1994.
49. L.F. Mondolfo: *Aluminum Alloys: Structure and Properties*, Butterworth and Co., Boston, 1976.
50. H.J. Frost and M.F. Ashby: *Deformation Mechanism Maps*, Pergamon Press, Elmsford, NY, 1982.